Simulation of ship motion response in head seas using a fully nonlinear potential flow method

Kaiyuan Shi[a], Renchuan Zhu[a,*], Minmin Zheng[b] and Chuanqing Li[a,b]

[a]State Key Laboratory of Ocean Engineering, School of Ocean and Civil Engineering, Shanghai Jiao Tong University, Shanghai, 200240, China
[b]State Key Laboratory of Navigation and Safety Technology, Shanghai Ship & Shipping Research Institute Co., Ltd., Shanghai, 200135, China

ARTICLE INFO

Keywords:
Fully nonlinear potential flow
KRISO Container Ship
Seakeeping
Motion response
Parametric rolling

ABSTRACT

This study develops a novel fully nonlinear potential flow approach for predicting the seakeeping performance of the KRISO Container Ship (KCS). We utilize a spectral coupled boundary element method for enhanced numerical efficiency and an acceleration potential-based technique for six degrees of freedom (6-DoF) motion calculation, together facilitating accurate simulations of ship-wave interactions. An overset mesh technique and an automated mesh-cutting process are introduced to accurately model instantaneous boundaries. Convergence analyses are conducted to validate the proposed method. Simulations of heave and pitch responses in head waves show good agreement with experimental and computational fluid dynamics results in literature, also demonstrating the nonlinear effects of large incident waves on ship motion. Moreover, the method accurately simulates parametric rolling and reveals the coupling effect between roll and other DoFs.

1. Introduction

Seakeeping performance, reflecting a ship's ability to function effectively at sea, is crucial for ship design and operation. Precise analysis of a ship's motion and forces in waves not only helps in designing vessels that are more comfortable and energy-efficient but also guides their safe navigation. This leads to fewer maritime accidents, better energy efficiency, and increased operational reliability. Such advancements require an in-depth understanding of ships' hydrodynamic behaviors. Thus, developing accurate and reliable seakeeping prediction methods carries significant value in naval architecture and ocean engineering, both theoretically and practically.

Model tests are often considered the most reliable approach to studying seakeeping performance. Through experiments with scaled ship models in controlled settings, researchers can meticulously examine the ship's behavior under specific wave conditions. Over the years, numerous seakeeping tests have been conducted on various benchmark models. Distinct from ship hulls like Wigley and Series 60, the KRISO Container Ship (KCS) model has more of the characteristics of a modern ship, with complex designs such as bulbous bows and transom sterns. Simonsen et al. (2013) studied the KCS's motions and resistance in calm water and head seas through experimental studies. Sadat-Hosseini et al. (2015) investigated the effects of different wave headings on the KCS's motion response and added resistance. Wu et al. (2020) examined the forces, motion responses, and wake fields of the KCS in waves. Shivachev et al. (2020) assessed the added resistance and motion response of the KCS under varying trim angles. Apart from motion response and added resistance, parametric rolling, a severe nonlinear phenomenon characterized by large amplitude rolling due to parametric resonance in head seas, also has gained extensive research focus. Yu et al. (2018) conducted experiments on parametric rolling in both regular and irregular head seas, proposing early detection algorithms and rudder stabilization strategies. Tello Ruiz et al. (2019) delved into the parametric rolling phenomenon of the KCS hull in shallow water, employing both numerical and experimental methods to uncover the influence of shallow water on parametric rolling dynamics.

While model tests stand as a highly reliable approach for seakeeping analysis, its drawbacks include high costs, time requirements, and potential limitations in capturing hydrodynamic characteristics. Consequently, numerical simulation emerges as a cost-effective and accessible alternative for seakeeping studies. A prevalent technique in engineering for seakeeping forecast employs the linear potential flow method. For instance, Bhatia et al. (2023) used the strip theory software MaxSurf to predict the heave, pitch, and roll of the KCS under various speeds and wave headings.

*Corresponding author
aeonic@sjtu.edu.cn (K. Shi); renchuan@sjtu.edu.cn (R. Zhu)
ORCID(s): 0000-0002-5103-8928 (K. Shi); 0000-0003-0689-9064 (R. Zhu)

Liang et al. (2024) conducted an investigation into the time history of ship wakes detected by a stationary observer as ships passed by. Xu et al. (2023) applied a frequency-domain, three-dimensional pulsating and translating Green's function to obtain the motion response of various ship hulls, including the KCS. However, the linear potential flow theory merely assumes small disturbances by minor incident waves near the average wetted surface of the hull, which diverges significantly from real-world. It neglects the disturbances caused by the steady ship wave on the free surface and the nonlinear effects of large incident waves and scattered waves, resulting in inaccuracies in simulating the motion response and capturing nonlinear phenomena such as parametric rolling. Therefore, researchers have devised several weakly nonlinear potential flow methods that incorporate factors such as steady ship wake and wetted surfaces. France et al. (2003) calculated Froude-Krylov forces and hydrostatic restoring forces on the instantaneous wetted surface, effectively simulating the parametric rolling of the C11 container ship. Zhang et al. (2018) achieved an accurate simulation of the KCS's motion response through a nonlinear time-domain potential flow method. Moreover, Zhang et al. (2023a) explored the parametric rolling characteristics of the KCS using a time-domain potential flow approach.

On the other hand, the Computational Fluid Dynamics (CFD) method that solves the Unsteady Reynolds-Averaged Navier-Stokes (URANS) equations, inherently accounts for viscosity effects and can robustly simulate strong nonlinearities, marking it as a crucial tool for seakeeping research. Many of the experimental studies mentioned above have employed URANS simulations for validation purposes (Simonsen et al., 2013; Sadat-Hosseini et al., 2015; Wu et al., 2020; Shivachev et al., 2020). Sulovsky et al. (2023) evaluated the accuracy of seakeeping predictions between the potential flow software WASIM and an OpenFOAM code using the URANS method, showing that WASIM's motion predictions deviated by about 30% from the experimental results, while OpenFOAM's predictions were in close agreement with the experimental data. Yu et al. (2023) performed simulations of the motion response and added resistance in different wave directions using the Spectral Wave Explicit Navier-Stokes Equations method. Furthermore, Wang et al. (2019); Wang (2020) investigated the parametric rolling of the KCS and the coupling effects of different modes with the in-house CFD code HUST-Ship.

In recent years, the Fully Nonlinear Potential Flow (FNPF) method has witnessed significant advancements. Compared to the linear or weakly nonlinear potential flow methods mentioned above, the FNPF method simulates the changing instantaneous wetted surface and nonlinear free surface in the time domain, which more closely aligns with physical reality. Compared to CFD methods that solve the N–S equations, the FNPF method simplifies the governing equations to the Laplace equation by by ignoring viscosity, thus striking a balance between computational efficiency and accuracy. Pacuraru et al. (2020) evaluated seakeeping simulations of the KCS using strip theory, FNPF software ShipFLOW Motions, and URANS software NUMECA, noting an increased significance of nonlinearity on motion response with higher speeds and wave heights. Studies by Coslovich et al. (2021) and Irannezhad et al. (2022) explored ship motion and resistance in waves using SHIPFLOW, while Tang et al. (2021) applied FNPF for simulating container ship motion in irregular waves. And Zhang et al. (2023b) studied the seakeeping of Wigley and S175, respectively. Furthermore, Tong et al. (2024) developed an adaptive harmonic polynomial cell method for nonlinear wave-structure interaction simulations. Although these FNPF methods have significantly outpaced URANS in terms of efficiency—improving by two to three orders of magnitude according to Irannezhad et al. (2022)—they still necessitate considerable computing time. For example, Tang et al. (2021) required 2-4 hours of parallel computing on a 6-core CPU for simulating a wave period using around 10,000 grids, and Irannezhad et al. (2022) needed 20 to 80 core-hours for a simulation with about 40,000 grids. This extensive computation is due to the FNPF method's requirement to account for the evolving free surface and wetted surface, solving the potential flow's boundary value problem (BVP) at each time step. To address this computational challenge, Shi et al. (2023) proposed a spectral coupled boundary element method (SCBEM) that introduces high-order spectral (HOS) methods to decompose the BVP, simplifying the boundary element method's (BEM's) solution and significantly enlarging the nonlinear computational domain while reducing the simulation time.

In light of the limitations of existing research, this paper aims to develop an FNPF method for accurate seakeeping simulations. Building on previous work with the SCBEM, this work introduces an acceleration potential method for the stable simulation of ships' six degree of freedom (6-DOF) motions, complemented by an automatic mesh method for modeling instantaneous surfaces. The simulations focus on the KCS hull's motion response in head seas. A thorough convergence analysis concerning mesh resolution, timestep size, and spectral coupling parameters confirms the method's validity. Remarkably, this method reduces the FNPF simulation time for a single wave period to less than one minute, while accurately predicting both the motion response in regular head seas and the parametric rolling of the KCS. This study of the KCS's parametric rolling using the FNPF method represents a novel contribution. Additionally, it explores the nonlinear effects of incident wave heights on motion response and the coupling effects between different motion modes during parametric rolling.

2. Fully nonlinear potential flow method

2.1. Coordinate systems

In this study, we employ two distinct coordinate systems to elucidate the flow field characteristics and the forces exerted on the ship hull:

- Earth-fixed coordinate system O–xyz: The origin of this coordinate system is situated at the calm water surface, with the z-axis oriented vertically upward. This stationary coordinate system is employed to describe the flow field, including the velocity potential and the wave elevation.
- Body-fixed coordinate system O'–$x'y'z'$: This coordinate system is attached to the ship hull and moves with the hull's oscillatory motion. The x'-axis is directed toward the bow, while the z'-axis extends vertically upward. This system is utilized for computing the 6-DoF motion equations of the ship.

At the initial instant, the two coordinate systems are aligned. To differentiate between them within this paper, the superscript $'$ is employed to signify quantities measured in the body-fixed coordinate system.

2.2. Governing equation and boundary conditions

In the context of a homogeneous, inviscid fluid and assuming irrotational flow, a velocity potential function ϕ exists that fulfills the Laplace equation:

$$\nabla^2\phi = 0 \tag{1}$$

The velocity field can be expressed as the gradient of ϕ:

$$\nabla\phi(x, y, z) = (u, v, w). \tag{2}$$

Presuming that the free surface remains non-overturning, the wave elevation can be represented as a single-valued function $\zeta(x, y)$ in the horizontal plane. On the free surface, ζ and ϕ must satisfy the following kinematic and dynamic conditions:

$$\frac{\partial\zeta}{\partial t} = \frac{\partial\phi}{\partial z} - \nabla_{\boldsymbol{x}}\phi \cdot \nabla_{\boldsymbol{x}}\zeta \quad \text{on } S_f \tag{3}$$

$$\frac{\partial\phi}{\partial t} = -\frac{|\nabla\phi|^2}{2} - g\zeta \quad \text{on } S_f \tag{4}$$

where $\nabla_{\boldsymbol{x}} \equiv (\partial/\partial x, \partial/\partial y)$ is the horizontal gradient operator, g the gravitational acceleration, and S_f the free surface. In a fully nonlinear simulation, the free surface's position varies temporally. Since Eq. (4) yields only the spatial derivative of the velocity potential from an Eulerian perspective, it necessitates an additional step to compute the temporal derivative of the velocity potential along the dynamic boundary. To address this, the velocity potential at the free surface, $\phi^S(x, y) = \phi(x, y, \zeta(x, y))$, is introduced. By substituting ϕ^S into the free surface boundary conditions and applying the chain rule, one derives the Zakharov form of these conditions (Zakharov, 1968):

$$\frac{\partial\zeta}{\partial t} = (1 + |\nabla_{\boldsymbol{x}}\zeta|^2)\frac{\partial\phi}{\partial z} - \nabla_{\boldsymbol{x}}\phi^S \cdot \nabla_{\boldsymbol{x}}\zeta \quad \text{on } S_f \tag{5}$$

$$\frac{\partial\phi^S}{\partial t} = \frac{1 + |\nabla_{\boldsymbol{x}}\zeta|^2}{2}\left(\frac{\partial\phi}{\partial z}\right)^2 - g\zeta - \frac{|\nabla_{\boldsymbol{x}}\phi^S|^2}{2} \quad \text{on } S_f \tag{6}$$

For the submerged hull surface, denoted as S_b, the fluid cannot penetrate the hull:

$$\frac{\partial\phi}{\partial n} = (\boldsymbol{U} + \boldsymbol{\Omega} \times \boldsymbol{r}) \cdot \boldsymbol{n} \quad \text{on } S_b \tag{7}$$

where $\boldsymbol{U}$ and $\boldsymbol{\Omega}$ represent the translational and rotational velocities of the ship, respectively, and $\boldsymbol{r}$ and $\boldsymbol{n}$ denote the position vector on the hull's surface and the outward unit normal vector, respectively.

In addition, the flow field must satisfy the deep-water bottom boundary condition:

$$\frac{\partial \phi}{\partial z} = 0 \quad \text{as } z \to -\infty \tag{8}$$

Equations (5)–(8) collectively constitute the boundary conditions within the FPNF framework. Given the initial wave elevation ζ and the velocity potential at the free surface ϕ^S, the evolution of nonlinear waves can be simulated by numerically integrating ζ and ϕ^S over time using methods such as the Runge–Kutta method. To calculate the $\partial\phi/\partial z$ term in Eqs. (5) and (6), one must solve the following BVP:

$$\begin{cases} \nabla^2 \phi = 0 & \text{in the fluid domain} \\ \phi = \phi^S & \text{on } S_f \\ \dfrac{\partial \phi}{\partial n} = (\boldsymbol{U} + \boldsymbol{\Omega} \times \boldsymbol{r}) \cdot \boldsymbol{n} & \text{on } S_b \\ \dfrac{\partial \phi}{\partial z} = 0 & \text{as } z \to -\infty \end{cases} \tag{9}$$

This paper employs the SCBEM (Shi and Zhu, 2023a) to solve the aforementioned BVP, which will be elaborated upon in Section 3.3.

2.3. Six degrees of freedom motion calculation

Considering the ship as a rigid body, its 6-DoF motion in the body-fixed coordinate system adheres to the Newton–Euler motion equations:

$$\boldsymbol{F}'_{\text{water}} + \boldsymbol{F}'_{\text{gravity}} + \boldsymbol{F}'_{\text{others}} = [\boldsymbol{M}] \begin{bmatrix} \dot{\boldsymbol{U}}' \\ \dot{\boldsymbol{\Omega}}' \end{bmatrix} + \boldsymbol{F}'_{\text{cc}} \tag{10}$$

Here, $[\boldsymbol{M}]$ is the mass-inertia matrix in the body-fixed coordinate system, $\dot{\boldsymbol{U}}'$ and $\dot{\boldsymbol{\Omega}}'$ denote the acceleration and angular acceleration in the body-fixed system, respectively, and $\boldsymbol{F}'_{\text{cc}}$ accounts for the Coriolis and centrifugal forces:

$$\boldsymbol{F}'_{\text{cc}} = \begin{bmatrix} m\boldsymbol{\Omega}^{\times} & -m\boldsymbol{\Omega}^{\times}\boldsymbol{c}^{\times} \\ m\boldsymbol{c}^{\times}\boldsymbol{\Omega}^{\times} & \boldsymbol{\Omega}^{\times}\left(\boldsymbol{I}_{\text{cm}} - m\boldsymbol{c}^{\times}\boldsymbol{c}^{\times}\right) \end{bmatrix} \begin{bmatrix} \boldsymbol{U}' \\ \boldsymbol{\Omega}' \end{bmatrix} \tag{11}$$

where m is the rigid body mass, $\boldsymbol{I}_{\text{cm}}$ is the moment of inertia about the center of mass, while $\boldsymbol{c}^{\times}$ and $\boldsymbol{\Omega}^{\times}$ are the matrix representations of cross products for $\boldsymbol{c}'$ and $\boldsymbol{\Omega}'$, respectively.

The external forces acting on the ship include the fluid pressure $\boldsymbol{F}'_{\text{water}}$, gravity $\boldsymbol{F}'_{\text{gravity}}$, and other constraint forces $\boldsymbol{F}'_{\text{others}}$. The fluid pressure is determined by integrating the pressure over the wetted surface of the hull:

$$\boldsymbol{F}'_{\text{water}} = \iint_{S_b} p \begin{bmatrix} \boldsymbol{n}' \\ \boldsymbol{r}' \times \boldsymbol{n}' \end{bmatrix} dS = \rho \iint_{S_b} \left(-\phi_t - \frac{1}{2}|\nabla\phi|^2 - gz\right) \begin{bmatrix} \boldsymbol{n}' \\ \boldsymbol{r}' \times \boldsymbol{n}' \end{bmatrix} dS \tag{12}$$

where $\phi_t = \partial\phi/\partial t$ is the time derivative of the velocity potential. It is evident that ϕ_t should satisfy the Laplace equation. For the sake of numerical simulation stability, this study calculates ϕ_t by solving the BVP. Differentiating both sides of Eq. (7) in the body-fixed coordinate system with respect to time, we obtain:

$$\frac{d}{dt}(\boldsymbol{n} \cdot \nabla\phi) = \frac{d}{dt}\left(\boldsymbol{n}' \cdot (\boldsymbol{U}' + \boldsymbol{\Omega}' \times \boldsymbol{r}')\right) = \boldsymbol{n}' \cdot (\dot{\boldsymbol{U}}' + \dot{\boldsymbol{\Omega}}' \times \boldsymbol{r}') \tag{13}$$

Expanding the left-hand term of Eq. (13), we derive:

$$\begin{aligned} &\frac{d}{dt}(\boldsymbol{n} \cdot \nabla\phi) = \nabla\phi \cdot \frac{d\boldsymbol{n}}{dt} + \boldsymbol{n} \cdot \frac{d\nabla\phi}{dt} \\ &= \nabla\phi \cdot (\boldsymbol{\Omega} \times \boldsymbol{n}) + \boldsymbol{n} \cdot \left(\frac{\partial \nabla\phi}{\partial t} + (\boldsymbol{V}_{\text{b}} \cdot \nabla)\nabla\phi\right) \\ &= \frac{\partial \phi_t}{\partial n} + \frac{\partial}{\partial n}(\boldsymbol{V}_{\text{b}} \cdot \nabla\phi) \end{aligned} \tag{14}$$

where $\boldsymbol{V}_{\mathrm{b}} = \boldsymbol{U} + \boldsymbol{\Omega} \times \boldsymbol{r}$ denotes the velocity of a point fixed in the body-fixed coordinate system as observed from the earth-fixed coordinate system. Substituting Eq. (14) into Eq. (13) and integrating with the free surface condition from Eq. (4), we establish the Dirichlet condition for the free surface and the Neumann condition for the body surface to obtain ϕ_t:

$$\begin{cases} \phi_t = -g\zeta - \dfrac{1}{2}\left|\nabla\phi\right|^2 & \text{on } S_f \\ \dfrac{\partial\phi_t}{\partial n} = \boldsymbol{n}' \cdot (\dot{\boldsymbol{U}}' + \dot{\boldsymbol{\Omega}}' \times \boldsymbol{r}') - \dfrac{\partial}{\partial n}(\boldsymbol{V}_{\mathrm{b}} \cdot \nabla\phi) & \text{on } S_b \end{cases} \tag{15}$$

In Eq. (15), $\boldsymbol{n}' \cdot (\dot{\boldsymbol{U}}' + \dot{\boldsymbol{\Omega}}' \times \boldsymbol{r}')$ represents the influence of the body's acceleration in the body-fixed coordinate system. The term $\partial(\boldsymbol{V}_{\mathrm{b}} \cdot \nabla\phi)/\partial n$ denotes the impact caused by the movement of the body boundary in the earth-fixed coordinate system, which is analogous to the m term in those frequency domain simulations. There are two numerical challenges when using Eq. (15) to solve for ϕ_t: the first is the interdependence between ϕ_t and acceleration. Calculating ϕ_t requires known acceleration, yet Eq. (10) necessitates fluid force to determine acceleration. The second challenge is that $\partial(\boldsymbol{V}_{\mathrm{b}} \cdot \nabla\phi)/\partial n$ involves the second-order derivatives of the velocity potential, which can be difficult to calculate accurately numerically.

To solve ϕ_t with precision and stability, we adopt a method based on the concept of acceleration potential (Cointe, 1991; Wu and Eatock Taylor, 1996), decomposing the $\partial\phi/\partial t$ term into six modal velocity potentials related to acceleration and one residual velocity potential:

$$\phi_t = \begin{bmatrix} \varphi_1 & \varphi_2 & \dots & \varphi_6 \end{bmatrix} \begin{bmatrix} \dot{\boldsymbol{U}}' \\ \dot{\boldsymbol{\Omega}}' \end{bmatrix} + \varphi_7 - \boldsymbol{V}_{\mathrm{b}} \cdot \nabla\phi \tag{16}$$

where φ_{1-6} are the acceleration potentials for six modes, satisfying the Laplace equation and the respective boundary conditions:

$$\begin{cases} \varphi_i = 0 & \text{on } S_f \\ \dfrac{\partial\varphi_i}{\partial n} = n_i & \text{on } S_b \end{cases}, \quad i = 1, \dots, 6 \tag{17}$$

where n_i is the generalized normal vector. Here, $(n_1, n_2, n_3) = \boldsymbol{n}$ denotes the outward normal vector of the hull surface, and $(n_4, n_5, n_6) = \boldsymbol{r} \times \boldsymbol{n}$ denotes the moment vector.

φ_7, as the residual, satisfies the following boundary conditions:

$$\begin{cases} \varphi_7 = -g\zeta - \dfrac{1}{2}|\nabla\phi|^2 + \boldsymbol{V}_{\mathrm{b}} \cdot \nabla\phi & \text{on } S_f \\ \dfrac{\partial\varphi_7}{\partial n} = 0 & \text{on } S_b \end{cases} \tag{18}$$

Substituting the decomposition from Eq. (16) into the pressure integration of Eq. (12), the water pressure in the body-fixed coordinate system is now expressed as:

$$\boldsymbol{F}'_{\text{water}} = \boldsymbol{F}'_{\mathrm{w}} - [\boldsymbol{\mu}] \begin{bmatrix} \dot{\boldsymbol{U}}' \\ \dot{\boldsymbol{\Omega}}' \end{bmatrix} \tag{19}$$

where $[\boldsymbol{\mu}]$ is the added mass matrix. The element μ_{ij} of matrix $[\boldsymbol{\mu}]$ in the ith row and jth column is given by:

$$\mu_{ij} = \iint_{S_b} \varphi_j n_i dS \tag{20}$$

and $\boldsymbol{F}'_{\mathrm{w}}$ is the part of the fluid pressure that is independent of acceleration:

$$\boldsymbol{F}'_{\mathrm{w}} = \rho \iint_{S_b} \left(\boldsymbol{V}_{\mathrm{b}} \cdot \nabla\phi - \varphi_7 - \frac{1}{2}\left|\nabla\phi\right|^2 - gz \right) \begin{bmatrix} \boldsymbol{n}' \\ \boldsymbol{r}' \times \boldsymbol{n}' \end{bmatrix} dS \tag{21}$$

Finally, the 6–DoF motion acceleration of the object is decoupled:

$$\boldsymbol{F}'_{\mathrm{w}} + \boldsymbol{F}'_{\text{gravity}} + \boldsymbol{F}'_{\text{add}} - \boldsymbol{F}'_{\text{cc}} = ([\boldsymbol{M}] + [\boldsymbol{\mu}]) \begin{bmatrix} \dot{\boldsymbol{U}}' \\ \dot{\boldsymbol{\Omega}}' \end{bmatrix} \tag{22}$$

2.4. Wave generation and absorption

As depicted in Fig. 1, the methodology presented in this paper implements a wave-making zone upstream and a wave-damping zone downstream to facilitate the generation and absorption of waves. In the wave-making zone upstream, the velocity potential and wave elevation are relaxed toward the theoretical solution at each time step, utilizing a ramp function for modulation:

$$\begin{aligned} \zeta &= \zeta + R(x)(\zeta_{\text{theory}} - \zeta) \\ \phi^S &= \phi^S + R(x)(\phi^S_{\text{theory}} - \phi^S) \end{aligned} \tag{23}$$

Here, ζ_{theory} and ϕ^S_{theory} represent the prescribed wave elevation and velocity potential, respectively. For the regular wave conditions considered in this study, we employ the fifth-order deep-water Stokes wave function. $R(x)$ denotes the ramp function, defined as:

$$R(x) = \exp\left(-\left(\frac{3x - 3x_{\text{gen}}}{l_{\text{gen}}}\right)^8\right) \tag{24}$$

where l_{gen} is the length of the wave-making zone, and x_{gen} is the central coordinate of this zone along the x-axis.

In the wave-damping zone downstream, a Rayleigh viscous term is introduced into the free surface dynamic condition to dissipate the waves:

$$\frac{\partial \phi^S}{\partial t} = \frac{1 + |\nabla_x \zeta|^2}{2}\left(\frac{\partial \phi}{\partial z}\right)^2 - g\zeta - \frac{|\nabla_x \phi^S|^2}{2} - \nu\phi^S \tag{25}$$

where ν signifies the Rayleigh viscosity. Within the damping zone, the viscosity coefficient ν increases quadratically relative to the distance from the start point of the wave damping zone, x_{damp}:

$$\nu(x) = \nu_0(x - x_{\text{damp}})^2 \tag{26}$$

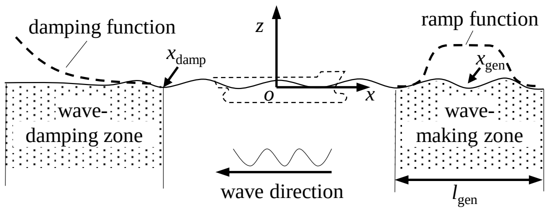

Figure 1: Schematic of the wave-making and damping zones.

3. Numerical implementation

3.1. Discretization of free surface nodes

This study utilizes discrete collocation points to represent the non-linear free surface. As a vessel progresses, the boundary topology of its associated flow field experiences temporal changes. To capture this dynamic behavior, our research implements the overset mesh technique to model the flow field of a ship in motion within an earth-fixed coordinate system. As shown in Fig. 2, the nodes located at a distance from the ship, referred to as background nodes, are arranged equidistantly and maintain fixed horizontal coordinates throughout the simulation, remaining static over time. In contrast, near the ship's hull, the free surface is not discretized by background nodes but by a set of unstructured points termed component nodes, which are generated automatically during the simulation.

To enhance the resolution of flow field details near the ship, component nodes are placed with a higher density than background nodes. The transfer of flow field information between different grids at each time step is achieved through radial basis function (RBF) interpolation techniques. Here, the thin-plate spline is chosen as the basis function.

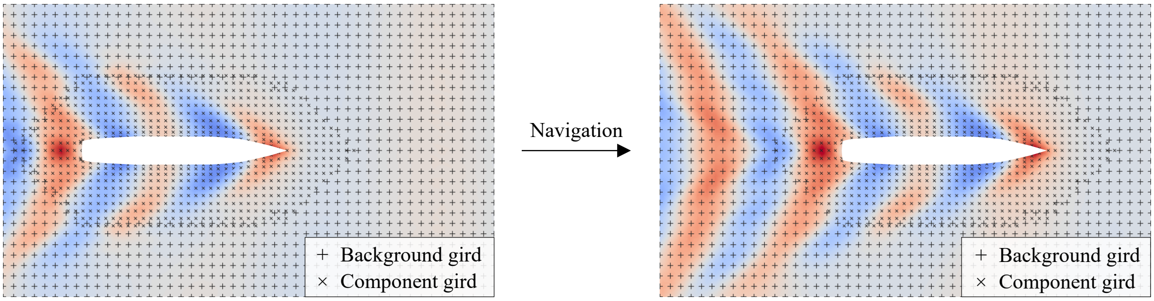

Figure 2: Distribution of free surface nodes at different times during ship navigation.

For each interpolation node, we use sample points within a radius of 3.5 grid lengths to construct the RBF surface for interpolation. In addition, wave breaking may occur in the numerical simulation, leading to potential flow model collapse. To maintain simulation, this study adopts a pre-breaking wave strategy by identifying nodes where the free surface mean curvature exceeds 1.8 as potential wave breaking points. These points are excluded during RBF surface construction to supress wave breaking. See Shi and Zhu (2023a) for more details.

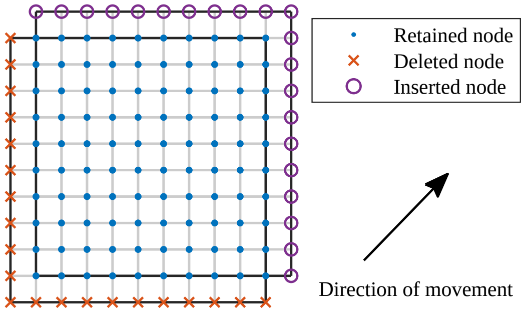

Figure 3: Schematic diagram of computational domain reconstruction.

In ship navigation simulations, using a fixed computational domain tied to an earth-fixed coordinate system poses a problem: the ship would eventually leave the simulation area. To address this issue and allow for longer simulations, our approach incorporates a dynamic tracking mechanism for the ship's centroid. This mechanism is activated when the ship's centroid moves more than one grid length away from the domain's center. Upon such deviation, a domain reconstruction process is initiated, which entails the deletion of background nodes that no longer align with the ship's trajectory and the generation of new background nodes in the ship's forward path, as shown in Fig. 3. In this way, the computational domain effectively achieves overall movement by selectively adding and removing nodes, rather than shifting the entire grid. This approach helps maintain computational accuracy, avoiding the errors that would come with simply moving the grid.

3.2. Update of instantaneous boundaries

In nonlinear potential flow simulations, the boundaries of the flow field, including the free surface and the instantaneous wetted surface, continuously change. Traditional methods typically adopt an explicit approach to track the movement of waterline nodes and determine the specific shape of the instantaneous wetted surface and free surface based on the waterline. However, this practice not only is challenging to apply to ship hulls with complex shapes but also tends to induce numerical instability. Contrary to these methods, our approach does not directly monitor waterline nodes. Instead, it implicitly determines the shape of the waterline based on the ship's attitudes and the free surface's position.

Figure 4 illustrates the process of updating the waterline using the method proposed in this study. We discretize the free surface with a set of scattered points. The wave elevation ζ and the velocity potential ϕ^S on the free surface are updated according to the Zakharov form of the free surface conditions, as specified in Eqs. (5) and (6). This method

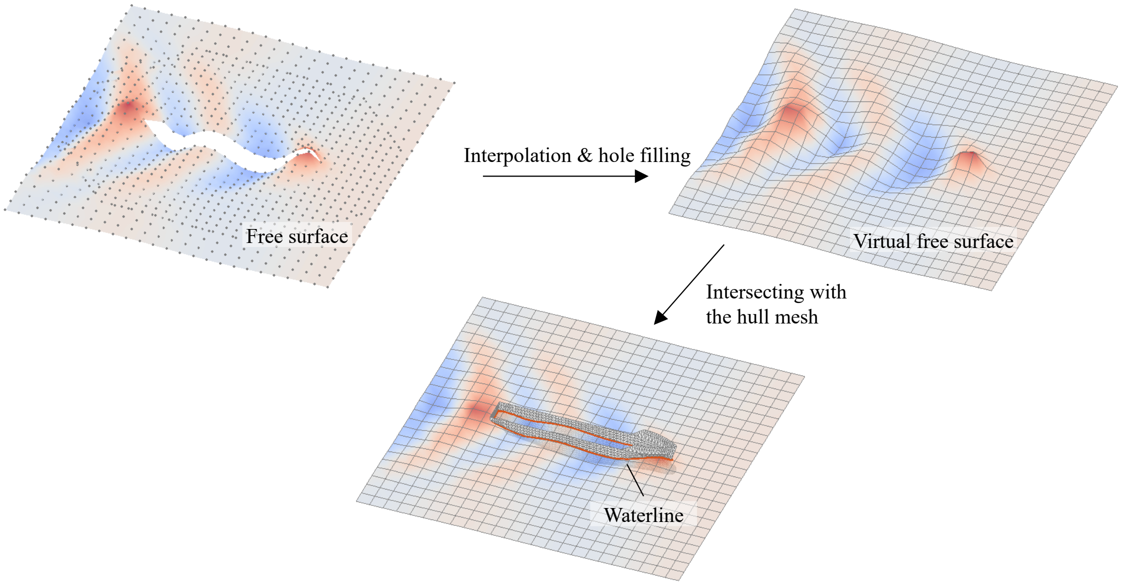

Figure 4: Schematic of waterline update steps.

allows the nodes to move vertically with the free surface, while their horizontal movement is restricted. Consequently, even though the flow field for the next timestep is computed, it is still represented using the grid from the previous timestep. This can lead to a mismatch between the grid and the actual boundaries for the upcoming timestep.

To address this, we apply RBF interpolation to the free surface on a uniform grid at the end of each timestep. Specifically, for each edge node within the voids uninterpolated due to the hull's presence, we construct an RBF surface using surrounding sample points in a 7×7 grid and extrapolate to determine the node's value. This iterative process continues until all voids are filled, resulting in a seamless *virtual free surface*, as illustrated in Fig. 5. The full hull mesh is intersected with this virtual free surface to establish the new waterline for the upcoming timestep. Based on the position of this waterline, the method automatically generates nodes for the free surface component outside the waterline and a mesh for the wetted surface below it, accurately reflecting the current physical boundaries. These meshes are then employed in the numerical calculations.

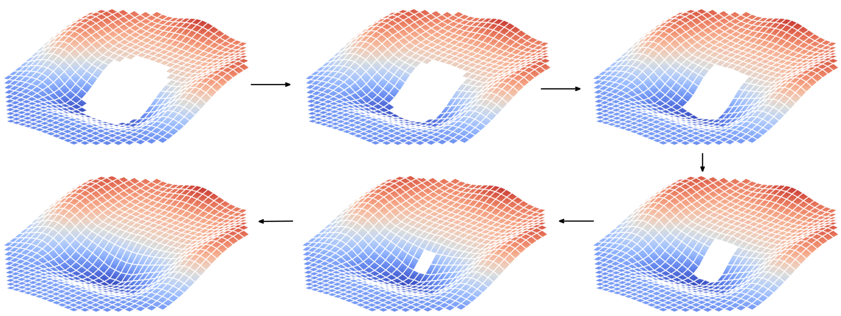

Figure 5: Progressive interpolation of virtual free surface.

Figure 6 depicts the algorithm used in this study to determine the instantaneous wetted surface panels. As demonstrated in Fig. 6(a), the process begins by vertically projecting the vertices of all panels onto the virtual free surface to identify the intersection points with the panel edges. If an intersection occur close to a panel vertex, that vertex is moved to the intersection. In cases where a vertex is proximate to several intersections, illustrated in Fig. 6(b), we reposition it to the median of these points. This adjustment of nodes ensures that most panels, which previously intersected the free surface, now have vertices exactly aligned with it, thereby reducing further intersections. Any

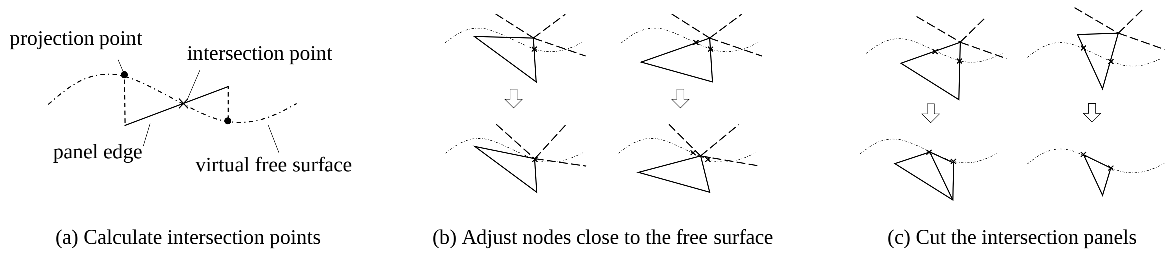

Figure 6: Procedure for generating the instantaneous wetted surface mesh.

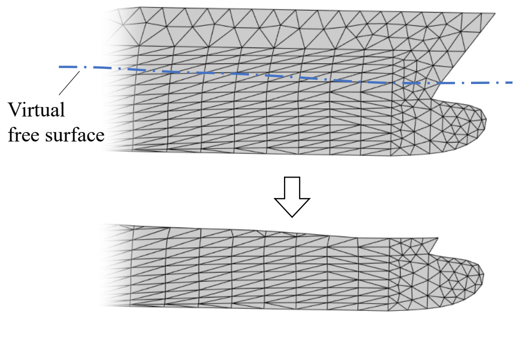

Figure 7: Instantaneous wetted surface mesh produced by the proposed method.

remaining panels that continue to intersect the free surface are then subdivided. Figure 7 showcases the success of this approach in creating an instantaneous wetted surface.

3.3. Spectral coupled boundary element method

Conventional BEMs necessitate the reconstruction and resolution of the boundary integral equation at each time step to accommodate the evolving boundaries. This process becomes exceedingly time-consuming when dealing with a large number of unknowns on the free surface. To improve efficiency, this paper adopts the SCBEM to solve the BVP of Eq. (9).

SCBEM leverages the linearity of the Laplace equation to split the mixed Dirichlet-Neumann BVP into two simpler sub-problems. It begins by defining a rectangular region around the ship body, termed the coupling region, and introduces a transition function $\mathcal{T}$:

$$\mathcal{T} = \begin{cases} 1 - T_x T_y & \text{in the coupling region} \\ 1 & \text{outside the coupling region} \end{cases} \tag{27}$$

Within the coupling region, T_x and T_y are given by:

$$\begin{aligned} T_x &= \frac{1}{2}\left(\operatorname{erf}\left(\frac{4d_x}{l_x} - 2\right) + 1\right) \\ T_y &= \frac{1}{2}\left(\operatorname{erf}\left(\frac{4d_y}{l_y} - 2\right) + 1\right) \end{aligned} \tag{28}$$

where erf is the Gauss error function, d_x and d_y are the distances from a point to the nearest horizontal boundary along the x-axis and y-axis, respectively, while l_x and l_y denote the widths of the transition zone, as shown in Fig. 8. The transition function $\mathcal{T}$ remains zero within the interior of the coupling domain and smoothly transitions from 0 to 1

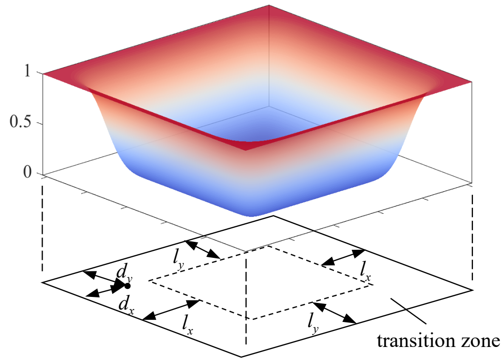

Figure 8: The distribution of the transition function within the coupling region.

within the transition zone. Utilizing this transition function, we can define a sub-problem as follows:

$$\begin{cases} \nabla^2 \phi_H = 0 & \text{in the fluid domain} \\ \phi_H = \mathcal{T} \phi^S & \text{on } S_{f*} \\ \dfrac{\partial \phi_H}{\partial z} = 0 & \text{as } z \to -\infty \end{cases} \tag{29}$$

Here, S_{f*} is the virtual free surface shown in Fig. 4. In this BVP, the velocity potential ϕ^S is undefined in the void caused by the presence of the ship hull, but since the transition function value is zero there, the Dirichlet condition can be treated as zero. Equation 29 presents a pure Dirichlet problem, which we refer to as the spectral layer. The spectral layer's Dirichlet problem is efficiently solved using a high-order spectral method (Dommermuth and Yue, 1987) with a time complexity of $O(N \log N)$.

Substituting the spectral layer velocity potential ϕ^H from Eq. (29) into Eq. (9), we determine the residual boundary conditions solved by the BEM:

$$\begin{cases} \nabla^2 \phi_R = 0 & \text{in the fluid domain} \\ \phi_R = (1 - \mathcal{T}) \phi^S & \text{on } S_f \\ \dfrac{\partial \phi_R}{\partial n} = -\dfrac{\partial \phi_H}{\partial n} + (\boldsymbol{U} + \boldsymbol{\Omega} \times \boldsymbol{r}) \cdot \boldsymbol{n} & \text{on } S_b \\ \dfrac{\partial \phi_R}{\partial z} = 0 & \text{as } z \to -\infty \end{cases} \tag{30}$$

The desingularized Rankine source method is used to solve for ϕ^R, with detailed numerical implementation in Shi and Zhu (2023a). The sum of ϕ_H and ϕ_R yields the velocity potential that satisfies the boundary conditions of Eq. (9).

Figure 9 depicts the SCBEM's decomposition strategy, where boundary colors reflect the magnitude of boundary values, and the gray area denotes a zero boundary value. The figure demonstrates that the introduction of a spectral layer significantly simplifies the original large-scale free surface Dirichlet-Neumann mixed BVP. Consequently, when using the BEM, there is no need to place Rankine sources throughout the entire domain, which substantially reduces computational efforts. In this paper's method, Rankine sources are only placed within the coupling region. The convergence analysis in Section 4.4 will confirm the validity of this approach.

4. Convergence analysis

4.1. Simulation setup

The numerical simulation focuses on the KCS model. In this study, propellers and rudders are not considered. Table 1 details the KCS hull's principal dimensions.

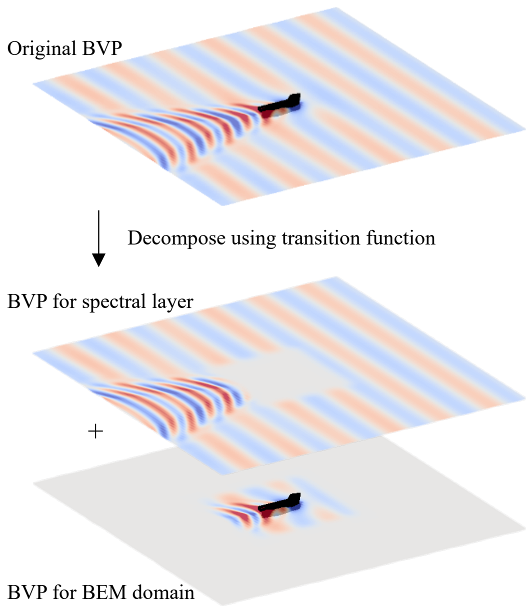

Figure 9: Decomposition strategy of the spectral coupled boundary element method (SCBEM), with colors indicating boundary value magnitudes.

Table 1
Principal dimensions of the KRISO Container Ship (KCS).

Principal Dimension	Symbol	Value
Length between perpendiculars	L_{pp} (m)	230
Maximum beam of waterline	B (m)	32.2
Draft	D (m)	10.8
Displacement volume	∇ (m^3)	52030
Block coefficient	C_{b}	0.6505
Longitudinal center of buoyancy	lcb (%L_{pp})	-1.48
Vertical center of gravity (from keel)	KG (m)	7.28
Moment of inertia	K_{xx}/B	0.324
	K_{yy}/L_{pp}	0.250

In the simulation, the ship is centrally placed within the computational domain. Artificial soft springs are applied in the surge DoF to permit free surge movement. The ship is unrestrained in heave and pitch DoFs. It begins from rest, accelerates to its design cruise speed corresponding to a Froude number of $F_n = 0.26$ with an acceleration of $0.1g$, and then proceeds at constant speed. Subsequently, the wave-making zone starts generating regular head-sea waves. For the convergence analysis, the incident wave has a wavelength of $\lambda/L_{\mathrm{pp}} = 1.15$ and a height of $H = 0.4$ m.

4.2. Mesh resolution dependency

Three sets of meshes with different densities are used to assess mesh independence. Figure 10 illustrates the hull mesh and the initial distribution of near-field free surface nodes for these meshes. Table 2 provides the node and panel counts for each mesh.

Figure 11 shows the heave and pitch motion time histories simulated with the different meshes. The medium and fine meshes yield nearly identical results, while the coarse mesh produces slightly lower motion response amplitudes. Compared to the heave motion, pitch motion is more sensitive to mesh resolution, showing greater discrepancies across the meshes.

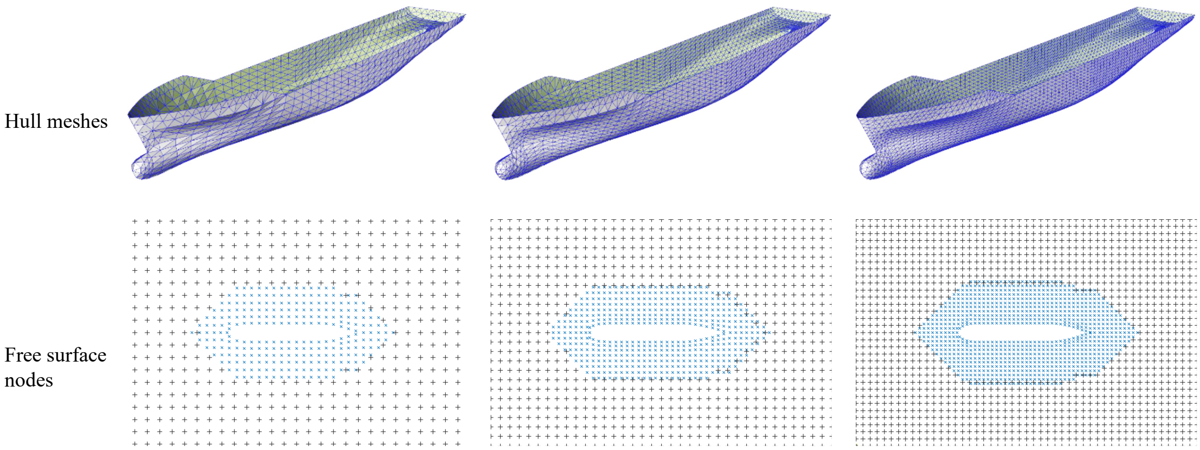

(a) Coarse mesh (b) Medium mesh (c) Fine mesh

Figure 10: Hull surface panels and free surface node distributions at varying mesh resolutions.

Table 2
Mesh parameters for three different resolutions.

	Coarse	Medium	Fine
Number of hull surface panels	1812	3520	6612
Number of background nodes	512×512	512×512	512×512
Spacing between background nodes	21.0 m	16.0 m	12.0 m
Number of component nodes	230	448	860
Spacing between component nodes	12.6 m	9.6 m	7.2 m

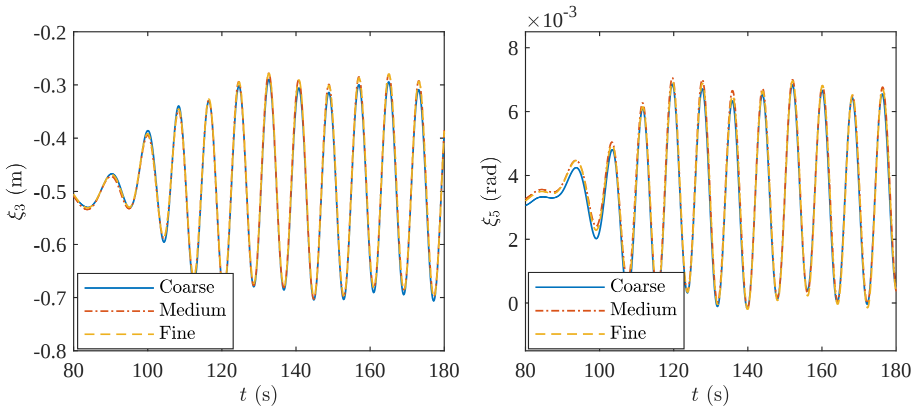

(a) Heave (b) Pitch

Figure 11: Time history of motions with different mesh resolutions.

The motion time histories depicted in Fig. 11 are not simple harmonic due to the disturbance waves created by the ship's acceleration from rest and the time required to reach a periodic steady state after encountering incident waves. For the subsequent response amplitude operators (RAOs) analysis, only the results approaching a steady state in the simulation will be selected for Fourier analysis.

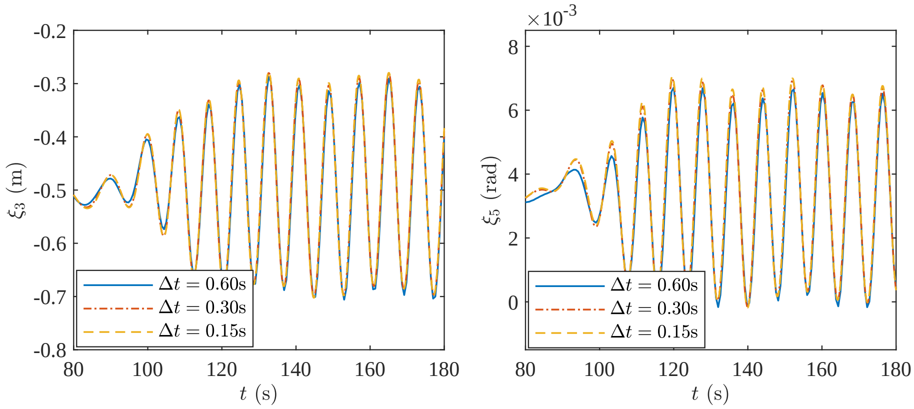

(a) Heave (b) Pitch

Figure 12: Motion time histories for different timestep sizes.

Table 3
Courant numbers and wave period to timestep ratios for various timestep sizes

Timestep size Δt	Courant number $U\Delta t/\Delta x$	Wave period/timestep $T/\Delta t$	Encounter period/timestep $T_e/\Delta t$
0.15 s	0.193	86.8	54.0
0.30 s	0.386	43.4	27.0
0.60 s	0.772	21.7	13.5

4.3. Timestep size dependency

Simulations with varying timestep sizes were conducted based on the medium mesh. Table 3 lists ratio of the wave period to the timestep size, along with the Courant number, which is the ratio of the ship's travel distance per timestep to the spacing between component nodes. In table 3, the natural period of the wave is denoted as T, while the encounter wave period is denoted as T_e. In the present method, the simulation is conducted in the earth-fixed coordinate system, with incident waves propagating forward according to their natural periods. Hence, the timestep size for simulating the incident wave field is related to the natural periods. Meanwhile, the scattered waves generated by the ship under the excitation of incident waves, as well as the ship's own motion, correspond to the encounter period. Therefore, the timestep size for simulating the motion is related to the encounter period. Figure 12 shows the time histories of the motion, demonstrating that the proposed method achieves rapid temporal convergence. The motion amplitudes from simulations with different timestep sizes are in good agreement. The minor discrepancies in the time histories at a timestep size of $\Delta t = 0.6$ s can be attributed to two factors: firstly, at this timestep size, there are only 13.5 timesteps within one encounter period, which may lead to larger errors in time-domain integration; secondly, a Courant number exceeding 0.5 may result in more significant mesh variations between consecutive timesteps and diminishes the accuracy of extrapolation (Shi and Zhu, 2023b).

4.4. Spectral coupling parameter dependency

The method used in this paper is based on the SCBEM, which simplifies the BVP in fully nonlinear simulations by introducing a spectral layer. It solves equations only within the coupling domain, avoiding the need to solve for all far-field discrete nodes. This efficiency allows for the simulation of a large nonlinear free surface with 250,000 nodes (512×512) without boundary reflection concerns due to a small computational domain. However, the numerical accuracy of this method must be assessed.

Using the medium mesh from Section 4.2 and a timestep size of $\Delta t = 0.3$ s, three sets of spectral coupling parameters were tested, as shown in Table 4. Sets I, II, and III progressively increase the coupling domain and transition zone sizes, resulting in longer times to solve the BEM coefficient matrix. The simulations were run on a PC with an AMD 3700X CPU and an RTX 2060 GPU, leveraging GPU acceleration technology for equation solving, as detailed in Shi and Zhu (2023a). The time cost per wave period for different spectral coupling parameters is also listed in Table

Table 4
Comparison of spectral coupling parameters across three sets.

	Set I	Set II	Set III
Coupling domain length	704 m	960 m	1600 m
Coupling domain width	704 m	960 m	1600 m
Transition region width l_x	128 m	192 m	320 m
Transition region width l_y	128 m	192 m	320 m
Initial BEM Unknowns	4940	7164	13940
Time cost per wave period	21.9 s	29.1 s	55.4 s

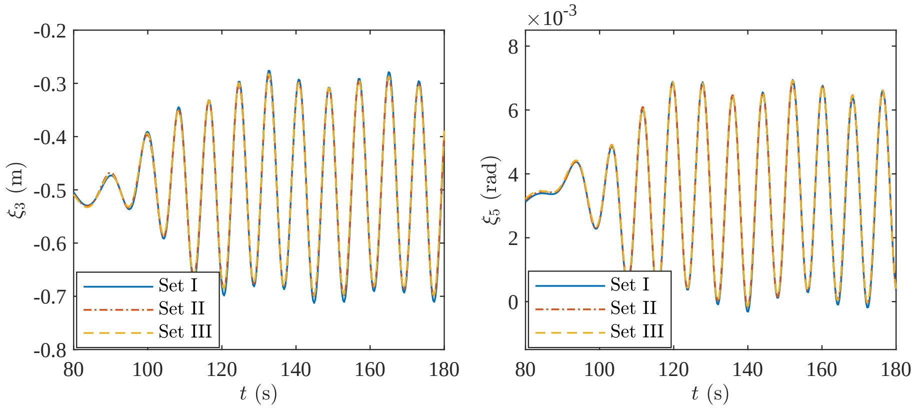

(a) Heave (b) Pitch

Figure 13: Time history of motions with different spectral coupling parameters.

4, demonstrating the method's high simulation efficiency, requiring only minutes to simulate motion response data suitable for Fourier analysis.

Figure 13 presents the motion responses simulated with the three parameter sets. The time histories agree well with each other, with the results from Sets II and III being almost indistinguishable and Set I's heave motion amplitude slightly higher. This suggests that the simulation can achieve adequate coupling with the parameters II and III used, and the size of the BEM computational domain (coupling domain) does not significantly affect the motion time history in the numerical simulation.

Figure 14 compares wave patterns simulated with different spectral coupling parameters. The wave patterns are consistent across different parameter sets, confirming that the SCBEM allows for nearly undisturbed wave propagation within the computational domain. As shown in Fig. 14(a), Set I solves the boundary element equation over an area of 704 m × 704 m, approximately twice the wavelength of the incident wave. Traditional BEMs would struggle to accurately simulate such conditions in such a limited domain without the spectral layer's assistance. Usually, the boundary's side wall effects and the requirements for wave generation and absorption would demand a larger computational domain for numerical simulation. However, SCBEM achieves accurate simulations with minimal error. This highlights the SCBEM's benefits: it not only significantly expands the computational domain but also reduces the computational load of FPNF simulations.

5. Heave and pitch responses in head waves

5.1. Response amplitude operator analysis

The incident wave heights $H = 0.4$ m and $H = 4.8$ m were chosen to simulate the motion response of KCS under regular wave conditions with varying wavelengths. For $H = 0.4$ m, the ratio $H/\lambda < 1/200$ for all simulated wavelengths, so the incident waves can be considered linear. In contrast, for $H = 4.8$ m, the ship experiences significant heave and pitch, revealing strong nonlinear effects. Figure 15 illustrates the RAOs obtained using the proposed nonlinear method, along with experimental and computational fluid dynamics (CFD) results from the literature. The

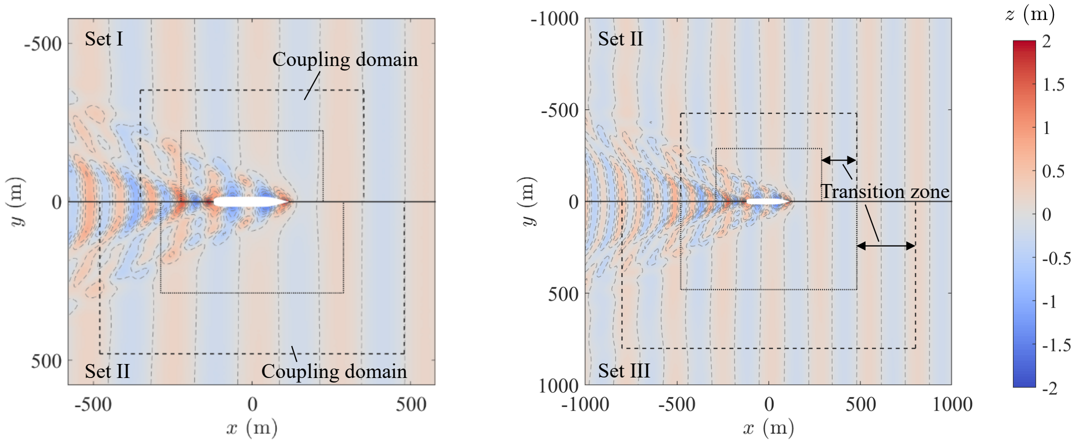

(a) Set I vs Set II
(b) Set II vs Set III

Figure 14: Wave patterns simulated with different spectral coupling parameters.

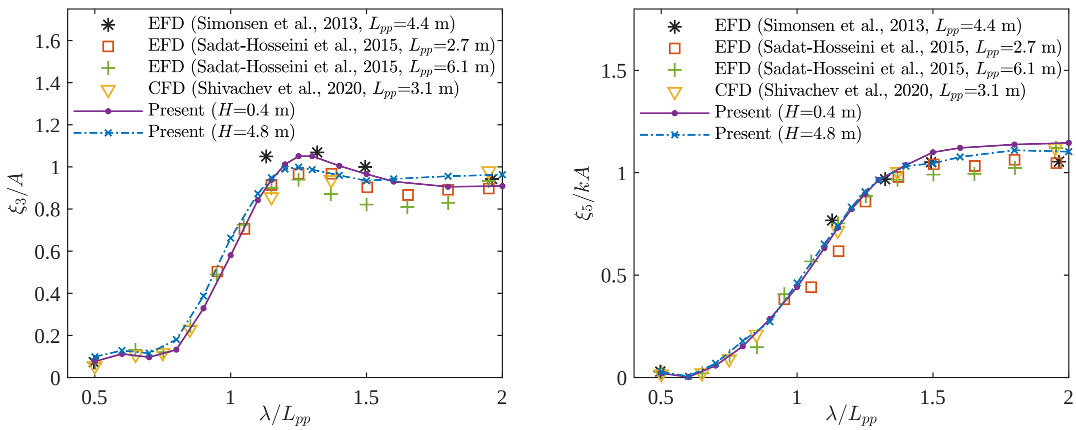

(a) Heave
(b) Pitch

Figure 15: Response amplitude operators for heave and pitch in head waves.

experimental data (EFD) includes model tests conducted by Simonsen et al. (2013) and Sadat-Hosseini et al. (2015) in the FORCE Technology towing tank, while the CFD results were obtained by Shivachev et al. (2020) using the STAR-CCM+ software.

Figure 15 demonstrates that the heave and pitch RAOs predicted by our numerical method agree well with those reported in the literature. The heave response is normalized by dividing by the incident wave amplitude A, and the pitch response is normalized by dividing by the product of the incident wave amplitude and the wave number kA. When compared to the experimental results by Sadat-Hosseini et al. (2015) and the CFD results, our potential flow approach tends to predict marginally higher heave and pitch RAOs within the range of $1 < \lambda/L_{\mathrm{pp}} < 2$. This discrepancy may arise from the potential flow simulation's limitation in capturing viscous effects, such as vortex shedding, which dampen the motion. The RAO curves predicted by our method distinctly illustrate the nonlinear effects on the motion response of the KCS. In shorter waves ($\lambda/L_{\mathrm{pp}} < 1$), the heave RAOs under large wave height is slightly larger compared to that under small wave excitation. However, the peak heave RAO at a high wave height of $H = 4.8$ m is about 5% lower than at a wave height of $H = 0.4$ m. As for the pitch RAO, differences between wave heights become apparent only for $\lambda/L_{\mathrm{pp}} > 1.5$, where the pitch RAO for steep waves is slightly lower compared to that for smaller amplitude waves.

5.2. Impact of large incident waves

To investigate the nonlinear effects of incident wave height on the motion response of the KCS, we conducted numerical simulations under three different wave conditions, with λ/L_{pp} ratios of 1.00, 1.25, and 2.00. It should be noted that our analysis is framed in potential flow theory and focuses on the effects of nonlinear free surface and significant changes in the wetted hull surface while omitting the influence of viscosity that might otherwise modify the wake pattern and ship motion.

Figure 16 presents the RAOs calculated by the proposed nonlinear method for various incident wave heights. The influence of wave height on RAOs does not follow a consistent trend across different wavelengths. Specifically, for the $\lambda/L_{\mathrm{pp}} = 1.25$ case, the heave RAO slightly decreases as wave height increases, whereas for the other two wavelengths, it slightly increases with wave height. The impact on pitch mode RAOs is less pronounced compared to that on heave.

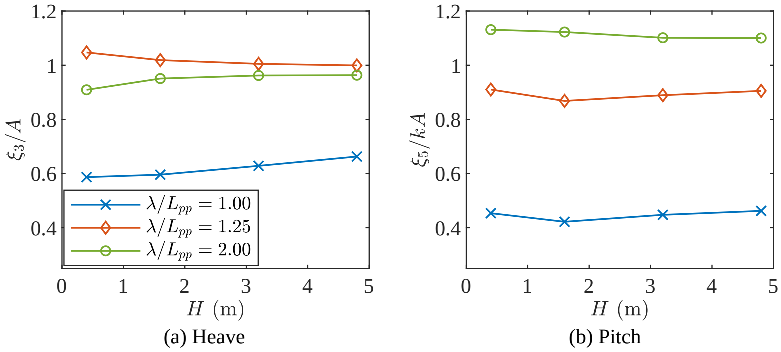

Figure 16: The variation of RAO with wave height for waves of different wavelengths.

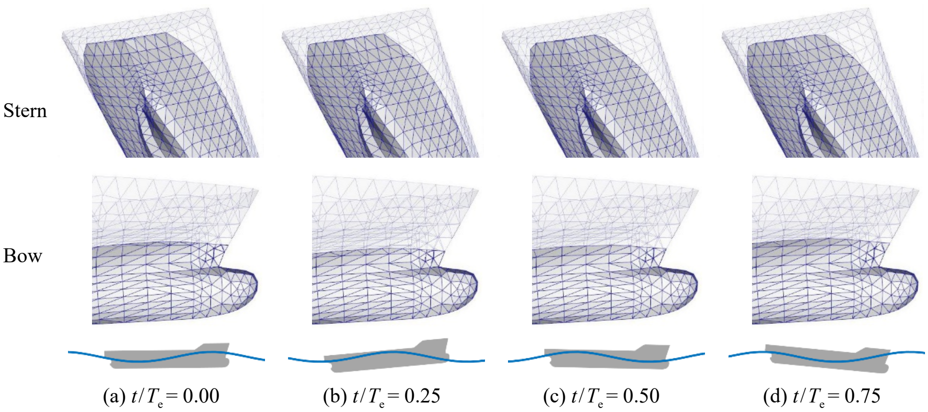

Figure 17: The instantaneous wetted surface changes of the bow and stern in the wave. ($\lambda/L_{\mathrm{pp}} = 1.25,\ H = 0.4m$)

Figures 17–19 present the instantaneous wetted surface meshes at different times after the simulation reached the steady state, with gray panels representing the submerged areas. The initial point $t/T_{\mathrm{e}} = 0$ corresponds to a pitch angle of zero. As Fig. 17 shows, for a wave height of $H = 0.4$ m, the wave's influence on the shape of the wetted surface is minor, resulting in a dry stern for the KCS hull, while the bulbous bow stays underwater. In contrast, with a wave height of $H = 4.8$ m, as shown in Figs. 18 and 19, there are considerable changes in the wetted surface. The transom stern does not consistently stay dry in such waves and may sporadically come into contact with water, with the bulbous bow also at risk of partially surfacing. The observed changes in the wetted surface are more evident for $\lambda/L_{\mathrm{pp}} = 1.25$ compared to $\lambda/L_{\mathrm{pp}} = 2.00$. This is because a ratio of $\lambda/L_{\mathrm{pp}} = 2.00$ corresponds to longer waves, which have a gentler wave slope for the same wave height. Consequently, the ship's movements are more in sync with these longer waves, leading to less relative motion between the ship and the water surface. In contrast, the ratio of $\lambda/L_{\mathrm{pp}} = 1.25$ causes

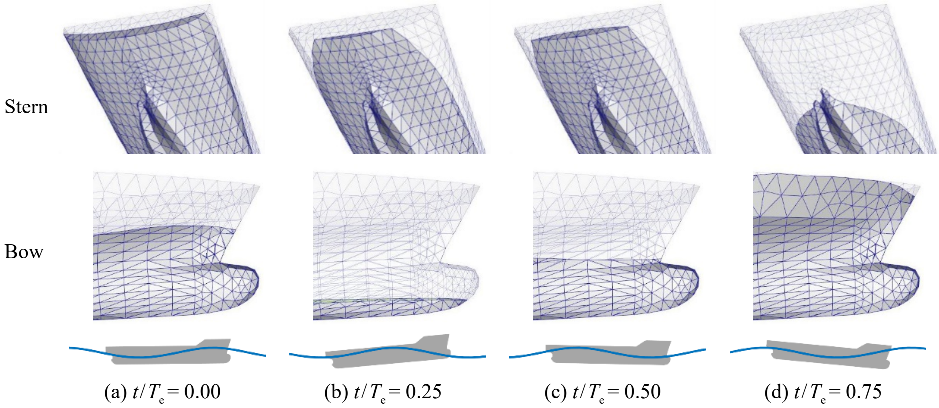

Figure 18: The instantaneous wetted surface changes of the bow and stern in the wave. ($\lambda/L_{pp} = 1.25,\ H = 4.8m$)

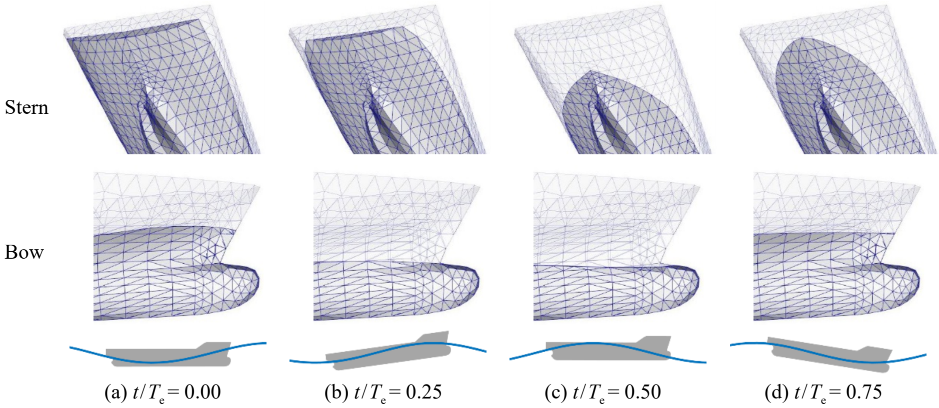

Figure 19: The instantaneous wetted surface changes of the bow and stern in the wave. ($\lambda/L_{pp} = 2.00,\ H = 4.8m$)

more pronounced changes in the ship's wetted surface due to their steeper slopes and the ship's more pronounced response to these wave patterns. Figure 20 further illustrates this effect, showing that the disturbance flow around the hull is significantly more intense under the $\lambda/L_{pp} = 1.25$ wave condition compared to $\lambda/L_{pp} = 2.00$.

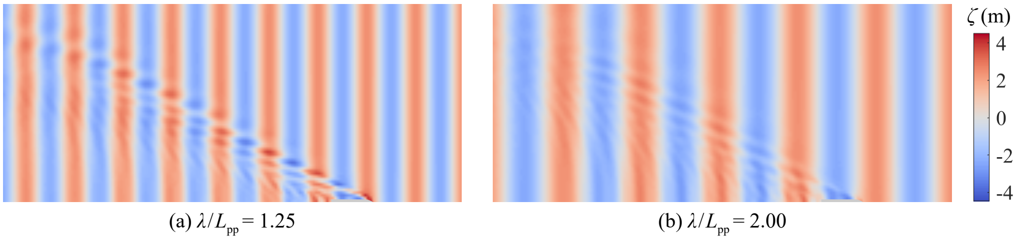

Figure 20: Far-field wave patterns under incident waves of different wavelengths (H = 4.8 m).

Table 5
Setup of KCS parameteric rolling test (in prototype scale).

	Case 5	Case 11
Wave length λ/L_{pp}	1.00	1.15
Wave steepness H/λ	0.02	0.02
Ship speed V	5 m/s	6 m/s
Natural roll period T_{roll}	19.97 s	19.97 s
Damping coefficient a	0.0336	0.0336
Damping coefficient b	0.0067	0.0067

6. Parametric rolling

6.1. Condition setting

Parametric rolling is a critical failure mode in the second-generation intact stability criteria adopted by the International Maritime Organization. In head seas, large waves can periodically alter the stiffness of the rolling restoring force, potentially causing severe parametric resonance in roll motion and even capsizing. This section presents a numerical simulation of the parametric rolling phenomenon for the KCS to validate the proposed method's ability to simulate strong nonlinear phenomena.

The numerical simulation setup in this section is refers to Cases 5 and 11 from setup II in the model test by Yu et al. (2019), using a ship model without bilge keels. Table 5 lists the specific parameters for the simulation cases. Since potential flow method do not account for viscous effects, roll damping might be underestimated. Therefore, an additional roll damping force is included in the motion equation:

$$M(\dot{\xi}_4) = -\frac{4a}{T_{\mathrm{roll}}} I'_{xx}\dot{\xi}_4 - \frac{3b}{4} I'_{xx}|\dot{\xi}_4|\dot{\xi}_4 \tag{31}$$

where I'_{xx} is the roll moment of inertia, $\dot{\xi}_4$ the roll angular velocity, T_{roll} the natural roll period, and a, b are the first and second-order damping coefficients, respectively, as listed in Table 5. The model test employed a self-propelled ship model, whereas the numerical simulation fixes the ship speed and constrains the yaw DoF to maintain heading, leaving all other DoFs free. Figure 21 shows the ship's attitude and wave pattern during simulation. It is evident that the wetted surface undergoes substantial changes under these conditions, which may result in a pronounced emergence of the bulbous bow.

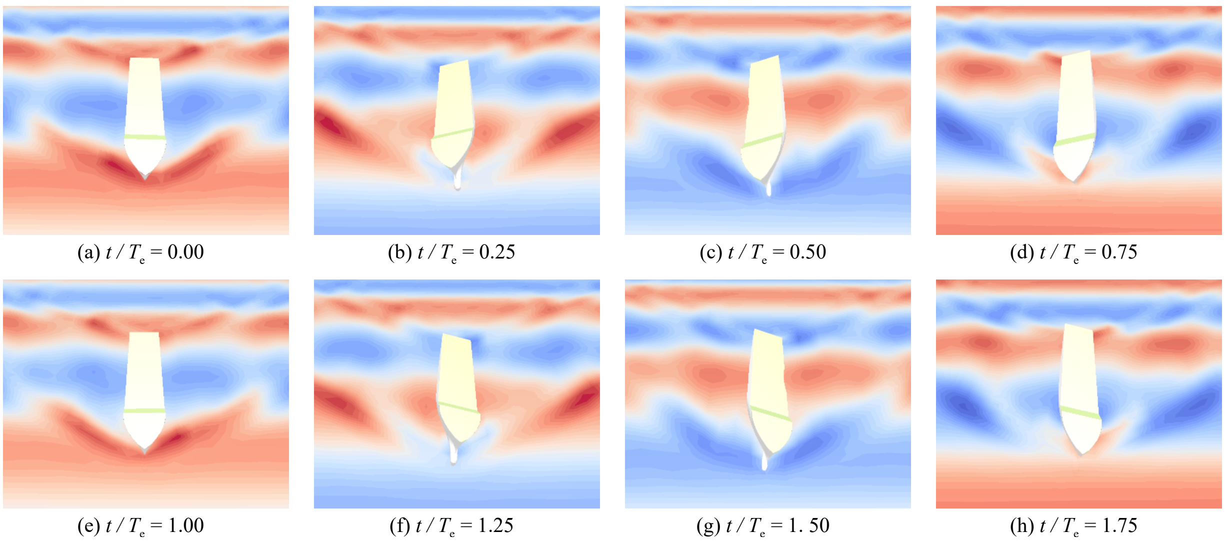

Figure 21: Ship attitude and wave pattern in the numerical simulation of parametric roll (Case 11).

6.2. Motion time history

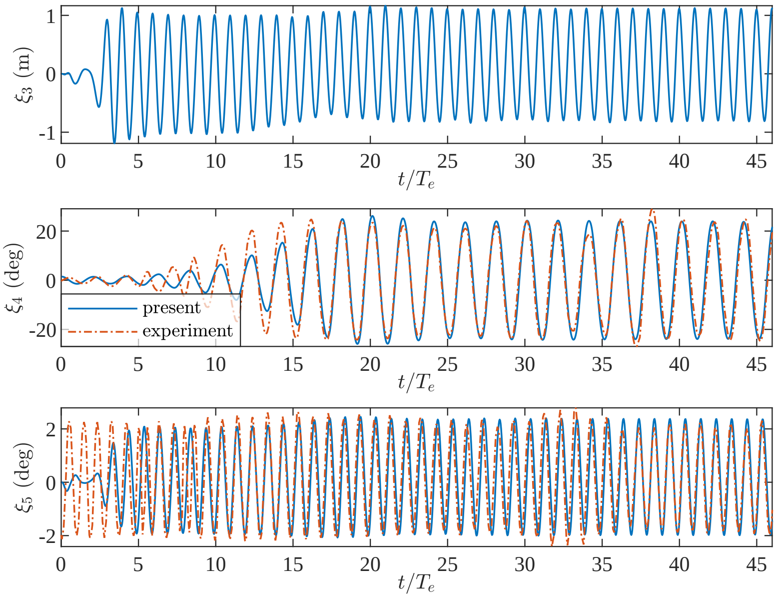

Figure 22: Time history of motion response for Case 5.

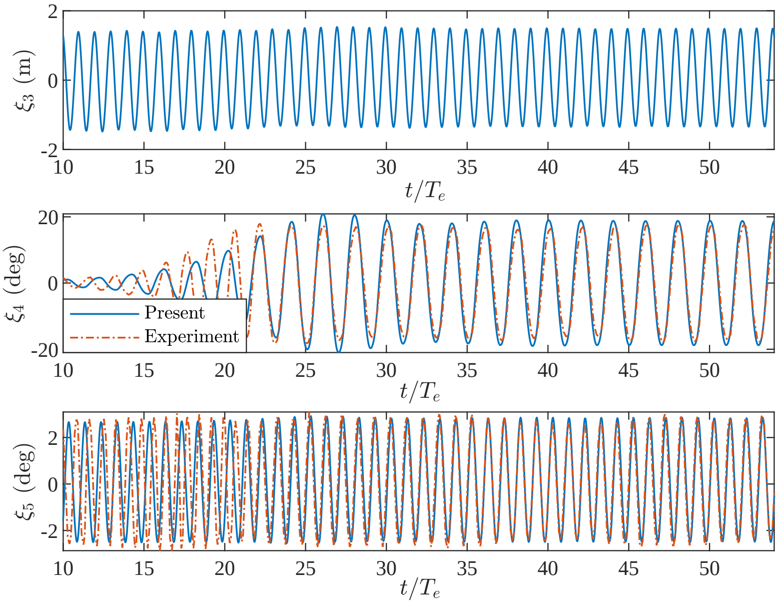

Figure 23: Time history of motion response for Case 11.

Figures 22 and 23 compare the motion time history of the numerical simulation with the experimental measurements. A positive pitch indicates bow trim, while a negative one indicates stern trim. For comparison, the time on the *x*–axis is nondimensionalized using the encounter wave period T_e. Phase differences between simulation and experiment may occur due to the challenge of maintaining a constant encounter period in the model test. As shown in Figs. 22 and 23, the fully nonlinear method accurately predicted the parametric rolling phenomenon, with the amplitude and phase of the roll and pitch motions closely matching experimental results. The simulated roll amplitudes for Cases 5 and 11 are 24.0 degrees and 18.7 degrees, respectively.

Additionally, the heave and pitch DoF exhibit coupling effects with the rolling motion. After the occurrence of parametric rolling, the ship's heave equilibrium position shifts slightly upwards, and a slight bow trim is observed in the pitch equilibrium position, similar phenomena could also be observed in the viscous numerical simulations by Wang (2020).

6.3. Attitude and restoring force

The periodic and significant changes in the roll restoring coefficient are commonly regarded as a primary cause of parametric rolling. For small-amplitude motion in mild waves, the roll restoring moment is directly proportional to the metacentric height GM_0 and the roll angle ξ_4:

$$M_{\text{res}}^{\text{linear}} = g\Delta GM_0\xi_4 \tag{32}$$

where Δ is the displacement. However, under large-amplitude waves, the ship's instantaneous wetted surface can differ markedly from the calm water condition. The hydrostatic restoring force is defined as the resultant of gravity and hydrostatic pressure on the instantaneous wetted surface:

$$M_{\text{res}}^{\text{nonlinear}} = M_{\text{roll}}^{\text{gravity}} + \rho \iint_{S_b} -gz\left(n_z y - n_y z\right) dS \tag{33}$$

A well-known simplified model for parametric rolling uses the Mathieu equation, assuming that the metacentric height oscillates with the incident wave. The Mathieu model's restoring moment is given by:

$$M_{\text{res}}^{\text{Mathieu}} = g\Delta GM(t)\xi_4 = g\Delta\left(GM_0 + GM_a\cos(\omega_{\text{e}}t)\right)\xi_4 \tag{34}$$

And the roll motion equation with linear damping becomes:

$$I'_{xx}\frac{d^2\xi_4}{dt^2} + 2\mu\omega_{\text{e}}I'_{xx}\frac{d\xi_4}{dt} + g\Delta GM(t)\xi_4 = 0 \tag{35}$$

where μ is the dimensionless linear damping coefficient. By defining $\phi_a = \xi_4\exp(\mu\tau)$, we can rewrite Eq. (35) as the standard Mathieu equation:

$$\frac{d^2\phi_a}{d\tau^2} + \left(p_4 + q_4\cos\tau\right)\phi_a = 0 \tag{36}$$

Here, $\tau = \omega_{\text{e}}t$ is the non-dimensional time, $p_4 = \Delta GM_0/(\omega_{\text{e}}^2 I'_{xx}) - \mu^2$ indicates the ratio of roll natural frequency to encounter frequency, and $q_4 = \Delta GM_a/(\omega_{\text{e}}^2 I'_{xx})$ measures the variability of the restoring stiffness with the wave presence. The stability diagram in Fig. 24 shows an unstable regions around $p_4 = 0.25$, where the encounter frequency is double the natural roll frequency. At these encounter frequencies, increased variation in the roll restoring stiffness heightens the risk of parametric rolling.

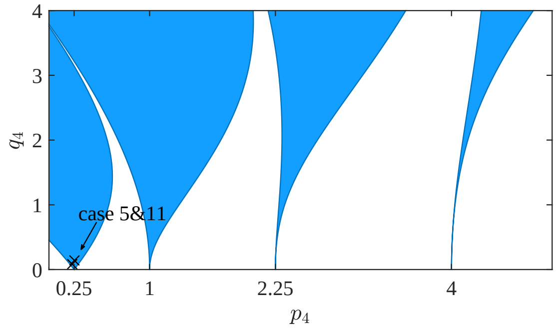

Figure 24: Ince-Strutt diagram. The shaded area indicates the unstable region of the Mathieu equation.

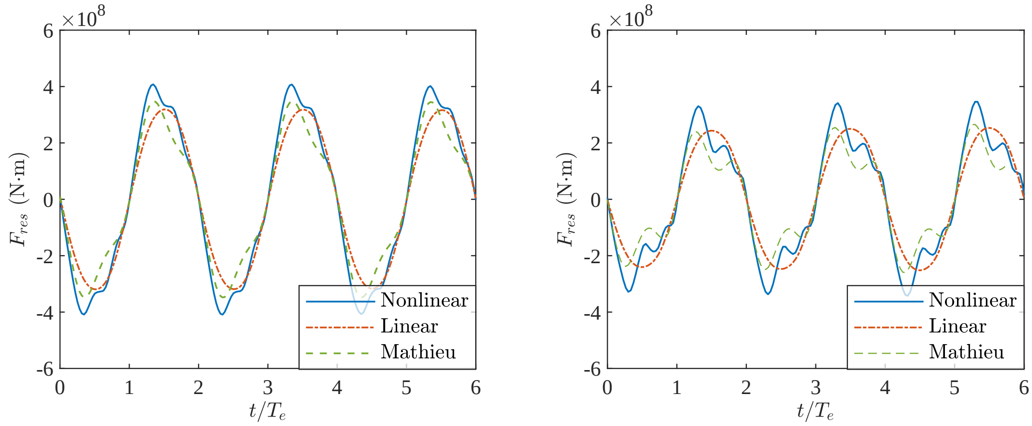

(a) Case 5 (b) Case 11

Figure 25: Comparison of nonlinear restoring force after periodic steady state with linear theory and Mathieu model.

Figure 25 presents the time history of the roll restoring moment calculated by the nonlinear potential flow method and compares it with linear theory and the Mathieu restoring force model. The GM_a in Eq. (34) is obtained by parameter identification of the nonlinear restoring force. The roll restoring moment exhibits clear nonlinear characteristics, notably the pronounced higher-order components. As depicted, the peak restoring moment occurs slightly before the maximum roll amplitude. However, the model in Eq. (34) falls short of fully capturing the nonlinear restoring force. The nonlinear restoring force tends to exceed calm water metacentric height estimates. This discrepancy is likely due to the asymmetry of the KCS hull and the interaction with other DoFs.

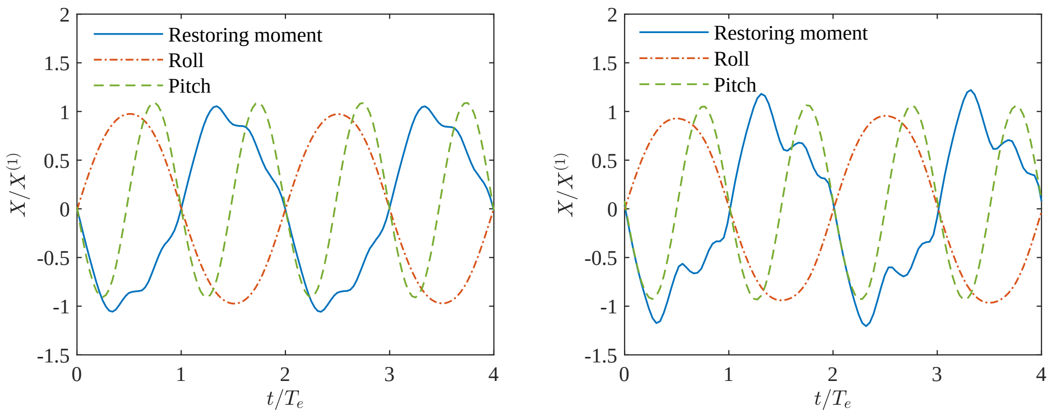

(a) Case 5 (b) Case 11

Figure 26: The phase relationship among roll restoring moment, roll, and pitch.

Figure 26 shows the phase relationship between the roll restoring moment, roll, and pitch. For comparison, all data are normalized by their first-order Fourier components. For Cases 5 and 11, it is observed that after reaching a periodic steady state, the KCS roll stabilizes at 0 degree simultaneously with the pitch approaching approximately 0 degrees. The roll restoring coefficient is generally higher when the ship trims by the stern than by the bow. Figure 27 explains this phenomenon by showing the KCS hull's instantaneous wetted surface at different times for Case 11. The stern of the KCS hull exhibits a pronounced flare, whereas the bow is more tapered. In a trim by stern condition, the roll motion induces significant changes in the waterline area at the stern, resulting in a large submerged area, a high moment of inertia for the waterplane, and consequently, a substantial roll restoring coefficient. Conversely, when the ship is in a trim by bow, the stern emerges markedly, reducing the moment of inertia of the waterplane and, therefore, diminishing the roll restoring force.

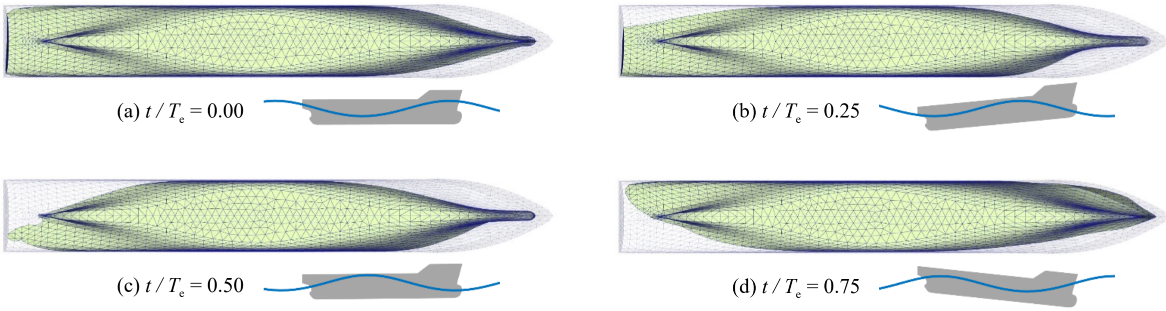

Figure 27: The instantaneous wet surface of the KCS hull at various times (Case 11).

7. Conclusion

This study presents an efficient FPNF method for seakeeping prediction. It employs the SCBEM for solving the BVP of nonlinear potential flow effectively. A technique based on acceleration potential is proposed to address the interdependency between acceleration and fluid forces, thus ensuring stable numerical simulation of the ship's 6-DoF motion. To accurately capture the dynamic changes in the flow field boundaries, the study develops an overset mesh method and an instantaneous wetted surface technique, which relies on node movement and panel cutting.

The validity of this method is confirmed through convergence analysis, examining the impact of varying grid resolutions, timestep sizes, and spectral coupling parameters. The results demonstrate good consistency across different settings. Particularly, the analysis focusing on spectral coupling parameters underlines the advantages of SCBEM, showcasing its capability to conduct nonlinear simulations across extensive computational domains with significantly lower computational demands compared to conventional approaches. Remarkably, simulating the KCS motion response takes less than one minute per wave period, highlighting the method's efficiency.

Further, the study performs nonlinear simulations to evaluate the KCS's heave and pitch motion responses in head waves. The RAO curves predicted from our method agree well with those from experimental and other CFD studies in existing literature. The simulations also illustrate the nonlinear effect of large incident wave heights on motion responses. Specifically, with larger waves, the heave RAO curve's peak value diminishes, and the shape of the instantaneous wetted surface undergoes more noticeable alterations.

Besides, the method precisely simulates the KCS's parametric roll, aligning the amplitude and phase of each DoF in the numerical simulations with model tests. The nonlinear simulations demonstrate the coupling effects between different motion modes; during parametric roll, the ship exhibits slight lifting and bow trimming. An analysis of the restoring force history and wetted surface attribute these phenomena to the asymmetry between the bow and stern. The KCS's flare stern provides a more substantial restoring force under parametric roll conditions, leading to the coupling effect.

The present method aims to provide an efficient and accurate tool for predicting seakeeping performance. However, it's important to note that this method has its limitations. As a potential flow method, it cannot accurately account for the effects of viscosity and wave breaking, and therefore has inherent limitations in simulating phenomena such as the wake of high-speed vessels and bow wave breaking. In addition, the method tracks the water surface based on the Zakharov form of the free surface condition, which doesn't allow overturning waves to be simulated. This raises questions about the accuracy of the simulation of slamming and green water. Our future work will include a detailed assessment of the effectiveness of the method in predicting added resistance, as well as investigating its validity in calculating slamming and green water loads.

Acknowledgments

The authors sincerely appreciate the support from the Fundamental Research Project of COSCO Shipping Co., Ltd. Author Kaiyuan Shi also wishes to thank the Startup Fund for Young Faculty at SJTU (SFYF at SJTU) for their valued funding.

References

Bhatia, M., Das, N., Dutta, P., Chattopadhyay, H., 2023. Numerical analysis on the seakeeping performances of a full-scale container ship hull using strip theory. Physics of Fluids 35.

Cointe, R., 1991. Nonlinear and linear motions of a rectangular barge in a perfect fluid, in: Proceeding of the 18th symposium on naval hydrodynamics, Washington DC. pp. 85–100.

Coslovich, F., Kjellberg, M., Östberg, M., Janson, C.E., 2021. Added resistance, heave and pitch for the kvlcc2 tanker using a fully nonlinear unsteady potential flow boundary element method. Ocean Engineering 229, 108935.

Dommermuth, D.G., Yue, D.K.P., 1987. A high-order spectral method for the study of nonlinear gravity waves. Journal of Fluid Mechanics 184, 267–288.

France, W.N., Levadou, M., Treakle, T.W., Paulling, J.R., Michel, R.K., Moore, C., 2003. An investigation of head-sea parametric rolling and its influence on container lashing systems. Marine Technology and SNAME news 40, 1–19.

Irannezhad, M., Eslamdoost, A., Kjellberg, M., Bensow, R.E., 2022. Investigation of ship responses in regular head waves through a fully nonlinear potential flow approach. Ocean Engineering 246, 110410.

Liang, H., Li, Y., Chen, X., 2024. An earth-fixed observer to ship waves. Journal of Fluid Mechanics 984, A14.

Pacuraru, F., Domnisoru, L., Pacuraru, S., 2020. On the comparative seakeeping analysis of the full scale KCS by several hydrodynamic approaches. Journal of Marine Science and Engineering 8, 962.

Sadat-Hosseini, H., Toxopeus, S., Kim, D.H., Castiglione, T., Sanada, Y., Stocker, M., Simonsen, C., Otzen, J.F., Toda, Y., Stern, F., 2015. Experiments and computations for KCS added resistance for variable heading, in: SNAME Maritime Convention, SNAME. p. D021S004R008.

Shi, K., Zhu, R., 2023a. Efficient spectral coupled boundary element method for fully nonlinear wave–structure interaction simulation. Physics of Fluids 35.

Shi, K., Zhu, R., Xu, D., 2023. A spectral coupled boundary element method for the simulation of nonlinear surface gravity waves. Journal of Ocean Engineering and Science .

Shi, K.y., Zhu, R.c., 2023b. A fully nonlinear approach for efficient ship-wave simulation. Journal of Hydrodynamics 35, 1027–1040.

Shivachev, E., Khorasanchi, M., Day, S., Turan, O., 2020. Impact of trim on added resistance of KRISO container ship (KCS) in head waves: An experimental and numerical study. Ocean Engineering 211, 107594.

Simonsen, C.D., Otzen, J.F., Joncquez, S., Stern, F., 2013. EFD and CFD for KCS heaving and pitching in regular head waves. Journal of Marine Science and Technology 18, 435–459.

Sulovsky, I., Hauteclocque, G.d., Greco, M., Prpić-Oršić, J., 2023. Comparative study of potential flow and CFD in the assessment of seakeeping and added resistance of ships. Journal of Marine Science and Engineering 11. doi:10.3390/jmse11030641.

Tang, Y., Sun, S.L., Ren, H.L., 2021. Numerical investigation on a container ship navigating in irregular waves by a fully nonlinear time domain method. Ocean Engineering 223, 108705.

Tello Ruiz, M., Villagomez, J., Delefortrie, G., Lataire, E., Vantorre, M., 2019. Parametric rolling in regular head waves of the KRISO container ship: numerical and experimental investigation in shallow water, in: International Conference on Offshore Mechanics and Arctic Engineering, American Society of Mechanical Engineers. p. V07AT06A064.

Tong, C., Shao, Y., Bingham, H.B., Hanssen, F.C.W., 2024. An adaptive harmonic polynomial cell method for three-dimensional fully nonlinear wave-structure interaction with immersed boundaries. Physics of Fluids 36.

Wang, S., 2020. An investigation into kcs parametric rolling through coupling different dofs, in: International Conference on Offshore Mechanics and Arctic Engineering, American Society of Mechanical Engineers. p. V008T08A043.

Wang, S., Wei, J., Chen, X., Liu, L., Zhang, Z., 2019. Numerical simulations of kcs parametric rolling in head waves, in: International Conference on Offshore Mechanics and Arctic Engineering, American Society of Mechanical Engineers. p. V002T08A039.

Wu, G.X., Eatock Taylor, R., 1996. Transient motion of a floating body in steep water waves, in: Proceeding of the 11th Workshop on Water Waves and Floating Bodies.

Wu, P.C., Hossain, M.A., Kawakami, N., Tamaki, K., Kyaw, H.A., Matsumoto, A., Toda, Y., 2020. EFD and CFD study of forces, ship motions, and flow field for KRISO container ship model in waves. Journal of Ship Research 64, 61–80.

Xu, D., Zhu, R., Zha, L., Wang, H., Li, C., 2023. Numerical investigation on three-dimensional radiated energy method and a new computation formula for total added resistance prediction. Ocean Engineering 271, 113734.

Yu, J., Yao, C., Wang, J., Liu, L., Dong, G., Zhang, Z., 2023. Numerical study on motion responses and added resistance for surge-free kcs in head and oblique waves based on the functional decomposition method. Ocean Engineering 285, 115300.

Yu, L., Ma, N., Wang, S., 2019. Parametric roll prediction of the KCS containership in head waves with emphasis on the roll damping and nonlinear restoring moment. Ocean Engineering 188, 106298.

Yu, L., Taguchi, K., Kenta, A., Ma, N., Hirakawa, Y., 2018. Model experiments on the early detection and rudder stabilization of kcs parametric roll in head waves. Journal of Marine Science and Technology 23, 141–163.

Zakharov, V.E., 1968. Stability of periodic waves of finite amplitude on the surface of a deep fluid. Journal of Applied Mechanics and Technical Physics 9, 190–194.

Zhang, B.J., Ning, X., et al., 2018. The research of added resistance in waves based on nonlinear time-domain potential flow theory. Journal of Marine Science and Technology 26, 6.

Zhang, W., Liu, Y.d., Chen, C., He, Y.p., Tang, Y.y., Sun, J.j., 2023a. Research on the parametric rolling of the kcs container ship. Journal of Marine Science and Technology 28, 675–688.

Zhang, X., Song, X., Beck, R.F., 2023b. Numerical investigations on seakeeping and added resistance in head waves based on nonlinear potential flow methods. Ocean Engineering 276, 114043.